Boosting the Self-Trapped Exciton Emission in Cs_4SnBr_6 Zero-Dimensional Perovskite via Rapid Heat Treatment

Haixia Wu , Zhenxu Lin , Jie Song , Yi Zhang , Yanqing Guo , Wenxing Zhang , Rui Huang *

Posted Date: 4 July 2023

doi: 10.20944/preprints202307.0071.v1

Keywords: photoluminescence; self-trapped exciton; Cs4SnBr6; rapid thermal treatment

Article

Boosting the Self-Trapped Exciton Emission in Cs_4SnBr_6 Zero-Dimensional Perovskite via Rapid Heat Treatment

Haixia Wu, Zhenxu Lin, Jie Song, Yi Zhang, Yanqing Guo, Wenxing Zhang and Rui Huang *

School of Materials Science and Engineering, Hanshan Normal University, Chaozhou 521041, China
* Correspondence: rhuang@hstc.edu.cn

Abstract: Zero-dimensional (0D) tin halide perovskites feature extraordinary properties, such as broadband emission, high photoluminescence quantum yield, and self-absorption-free characteristics. The innovation of synthesis approaches for high-quality 0D tin halide perovskites has facilitated the flourishing development of perovskite-based optoelectronic devices in recent years. However, discovering an effective strategy to further enhance their emission efficiency remains a considerable challenge. Herein, we report a unique strategy employing rapid heat treatment to attain efficient self-trapped exciton (STE) emission in Cs_4SnBr_6 zero-dimensional perovskite. Compared to the pristine Cs_4SnBr_6, rapid thermal treatment (RTT) at 200°C for a duration of 120 seconds results in an augmented STE emission with photoluminescence (PL) quantum yield rising from an initial 50.1% to a substantial 64.7%. Temperature-dependent PL spectra analysis, Raman spectra, and PL decay traces reveal that the PL improvement is attributed to the appropriate electron-phonon coupling as well as the increased binding energies of STEs induced by the RTT. Our findings open up a new avenue for efficient luminescent 0D tin-halide perovskites toward the development of efficient optoelectronic devices based on 0D perovskites.

Keywords: photoluminescence; self-trapped exciton; Cs_4SnBr_6; rapid thermal treatment

1. Introduction

In recent years, zero-dimensional (0D) metal halides have attracted significant attention due to their remarkable photoluminescence (PL) quantum yields (QY) and adjustable emissions. These materials, characterized by the confinement of luminescent metal halide octahedra by organic or inorganic cations, offer great potential for various optoelectronic applications, including LEDs, solar cells, scintillators, sensors, and thermal imaging systems [1–5]. In these materials, the Jahn-Teller distortion of metal halide octahedra upon photoexcitation leads to the localization of excitons, enhancing radiative emission by preventing exciton migration to defects. This phenomenon, known as self-trapping of excitons (STEs), contributes to high PL QY and improved stability [6,7]. While significant progress has been made in exploring efficient 0D metal halides, the use of lead-based compounds such as Cs_4PbBr_6 is limited by the toxicity of lead, posing environmental and health concerns [8–10]. To address this issue, tin (Sn^{2+}) has emerged as a promising alternative to lead (Pb^{2+}) due to its similar electronic properties and environmentally-friendly nature [11–13]. Numerous studies have probed into the intriguing properties of 0D tin halide perovskites, including Cs_4SnX_6 (where X = Br, I), and demonstrated their potential for optoelectronic applications [14–16]. For instance, the work conducted by Kovalenko and his team presented the compelling discovery of an efficient green-yellow emission derived from self-trapped excitons in Cs_4SnBr_6, with the achievement of a notable PL QY of 15±5% at room temperature [14]. Intriguingly, through strategic substitution of Cs^+ with Rb^+ or K^+ and Br^- with I^-, both the PL peak position and Stokes shift can be simultaneously adjusted [14]. Quan et al. synthesized high-quality Cs_4SnX_6 (X = Br, I) nanocrystals that exhibit well-defined shapes and narrow size distributions, culminating in an impressive PL QY of up to 21% for Cs_4SnBr_6 nanocrystals [16]. However, a persistent obstacle facing tin halide perovskites is their lack of stability in air, a problem primarily attributed to the oxidation of Sn^{2+} to Sn^{4+}, leading to a

 doi:10.20944/preprints202307.0071.v1

consequential decline in luminescent performance [17,18]. To overcome this issue, Zhang et al. implemented an innovative solution by introducing SnF_2 as a tin source, which replaced the easily oxidizable $SnBr_2$, and successfully enhanced the structural stability of Cs_4SnBr_6 perovskite by utilizing fluorine to suppress Sn^{2+} oxidation effectively [19]. Despite the remarkable PL performance displayed by 0D tin halide perovskites, the quest for their commercialization necessitates considerable efforts to further enhance both their PL efficiency and stability.

0D perovskites generally display wide-band emission with a large Stokes shift. Numerous researchers have employed the STEs model to elucidate the wide-band emission and large Stokes shift induced by octahedral distortions in 0D perovskites upon light excitation [20–24]. Strong electron-phonon coupling and a malleable lattice are widely considered the cornerstone factors driving the emission of STEs. Particularly within the context of 0D perovskites, excitons, when photoexcited, induce swift distortions in the lattice of the excited state, culminating in the formation of localized STEs [22–26]. Previous investigations have revealed that the lattice distortion in zero-dimensional metal halide perovskites can be manipulated by adjusting factors such as the chemical composition, temperature, and pressure. Such modulation enables precise control of the STE states, which in turn optimizes luminescence performance [22–27]. For example, the introduction of varying metal ions into 0D metal halide perovskites can amplify the distortion of $[BX6]^{4-}$ octahedra and bolster electron-phonon coupling, consequently enhancing the density of STE states and boosting luminescence efficiency [26]. In previous work, we successfully expanded the emission spectra and amplified the emission efficiency of STEs in Cs_4SnBr_6 through an innovative Mn^{2+} doping strategy [28]. This approach imbued the Mn^{2+}-doped Cs_4SnBr_6 with remarkably enhanced PL QY of up to ~75%, a broader emission spectrum, and increased thermal stability.

Rapid thermal treatment (RTT) is a widely used technique to modify the micro-nano structure and enhance the optoelectronic properties of materials [29]. RTT involves rapid heating and cooling, characterized by short heating times and accelerated cooling rates. This transient process can induce changes in the structural order of metal halide octahedra, which plays an important role in the formation of STEs. However, the influence of RTT on the PL properties of 0D Cs_4SnBr_6 has not been fully explored. In this study, we propose a novel strategy based on RTT to enhance the emission of STEs in lead-free Cs_4SnBr_6. We systematically investigate the effects of RTT on the optical properties of Cs_4SnBr_6. Compared to pristine Cs_4SnBr_6, we find that RTT at 200°C for 120 seconds leads to enhanced STE emission, with the PL QY escalating from an initial 50.1% to a substantial 64.7%. The improvement in PL is discussed in terms of electron-phonon coupling and increased binding energies of STEs induced by RTT.

2. Materials and Methods

Cs_4SnBr_6 samples were synthesized through water-assisted wet ball-milling. Cesium bromide (4 mmol, CsBr, Aladdin, 99.9%), stannous fluoride (1 mmol, SnF_2, Macklin, 99.9%), and ammonium bromide (1 mmol, NH_4Br, Aladdin, 99.99%) were employed as reactant precursors. To achieve Cs_4SnBr_6, the molar ratios of CsBr, SnF_2, and NH_4Br were maintained at 4, 1, and 2 mmol, respectively. Initially, the precursors were loaded into a jar and combined with 60 μL of deionized water. Subsequently, a ball milling process was conducted for 30 min at a speed of 600 rpm. The resulting product was then dried in a vacuum-drying oven for 120 min at room temperature and annealed at various temperatures ranging from 100 to 300 °C using a straightforward RTT process. The RTT process was executed on a rapid thermal processor, heating the sample to the annealing temperature at a rate of 10 °C s^{-1}. After maintaining the annealing temperature for 30, 90 and 120 s, respectively, the system was rapidly cooled to room temperature. Upon cooling, the Cs_4SnBr_6 powder was acquired via ball milling for 30 min at a speed of 600 rpm. PL measurements were conducted using an Edinburgh Instrument FLS1000 PL spectrometer (Livingstone, UK). The PL spectra were obtained at different temperatures to investigate the temperature-dependent behavior. PL excitation (PLE) spectra and time-resolved PL spectra were also recorded using the same instrument. The crystal structures of Cs_4SnBr_6 were analyzed using X-ray diffraction (XRD) with a Bruker D8 Advance instrument (Karlsruhe, Germany). XRD measurements were performed at 35 kV and 35 mA to

 doi:10.20944/preprints202307.0071.v1

determine the crystal structure of the samples. The compositions of Cs_4SnBr_6 were determined by energy dispersive spectroscopy (EDS) using a Bruker EDS QUANTAX system (Karlsruhe, Germany). Scanning electron microscopy (SEM) (A Hitachi SU5000 SEM instrument, Tokyo, Japan) was employed to investigate the surface morphology and microstructure of Cs_4SnBr_6.

3. Results and discussion

The PL spectra of pristine Cs_4SnBr_6 sample and samples subjected to RTT at different temperatures are shown in Figure 1(a). Both types of samples exhibited a broad emission with a peak at approximately 530 nm. The emission band had a large full width at half maximum (FWHM) of approximately 105 nm. Additionally, a significant Stokes shift of around 1.30 eV was observed, as illustrated in Figure 1(c) and 1(d). It is evident that RTT at temperatures below 150°C had minimal influence on the PL intensity of Cs_4SnBr_6 samples. However, a notable increase in PL intensity was observed when the RTT temperature was raised to 200°C. Conversely, as the RTT temperature was further increased to 300°C, the PL intensity of Cs_4SnBr_6 samples decreased rapidly. Figure 1(b) showcases PL spectra of Cs_4SnBr_6 samples annealed at a RTT temperature of 200°C over diverse durations. The observed PL intensity of the Cs_4SnBr_6 samples appears to increment gradually with the prolongation of RTT duration from 30 to 120 seconds. Notably, as depicted in Figures 1(e) and 1(f), the PL QY takes a significant leap from 50.1% to 64.7% following the annealing of the unprocessed Cs_4SnBr_6 at an RTT temperature of 200°C for a span of 120 seconds. Figures 2a and 2b display the excitation power dependence of PL for both the pristine sample and sample-120s. The insets of Figures 2a and 2b demonstrate that an increase in excitation power, from 160 to 2817 nW, is accompanied by a corresponding enhancement in PL intensity. Nevertheless, the PL peak position maintains consistent, unaffected by variations in the excitation power. Additionally, a distinct linear correlation emerges between the integrated PL intensity and the excitation power within the range of 160 to 2817 nW. The excitation power-dependent PL intensity is commonly employed to determine the underlying mechanism of light emission in semiconductors. As per the literature [30], the PL intensity (I) can be described by the equation $I = \eta I_0^k$, where I_0 denotes the excitation power, η symbolizes the emission efficiency, and the exponent k is affiliated with the radiative recombination process. A linear fit of $\ln(I/\eta)$ in contrast to $\ln(I_0)$ allows the estimation of the k parameter values as 1.11 and 1.17 for the pristine sample and sample-120s respectively. This deduction strongly suggests that the green emission in both samples is engendered by the recombination of excitons. Given the large Stokes shift of ~1.30 eV, coupled with a broad FWHM of the emission band approximating ~105 nm, and further considering the long radiative lifetime of ~1μs, as illustrated in Figure 5, the green emission can be ascribed to the radiative recombination STEs, which is prompted by Jahn–Teller distortion of $[SnBr_6]^{4-}$ octahedra in 0D perovskite [31–33].

Preprints (www.preprints.org) | NOT PEER-REVIEWED | Posted: 4 July 2023 doi:10.20944/preprints202307.0071.v1

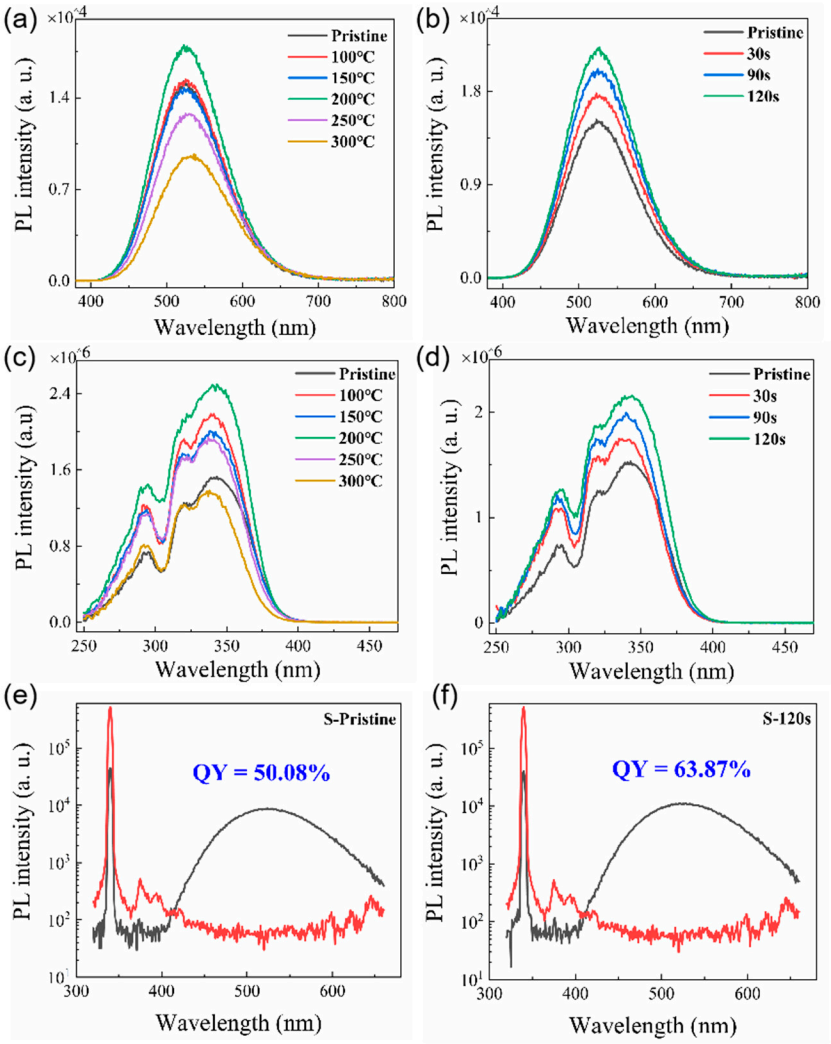

Figure 1. (a) PL spectra and (c) PLE spectra of both the unprocessed Cs_4SnBr_6 sample and samples treated with RTT at varying temperatures. (b) PL spectra and (d) PLE spectra of Cs_4SnBr_6 samples annealed at a RTT temperature of 200 °C for distinct durations. The PL QY derived from the excitation and emission spectra for (e) the pristine Cs_4SnBr_6, and (f) Cs_4SnBr_6 sample annealed at a RTT temperature of 200 °C for a span of 120 seconds.

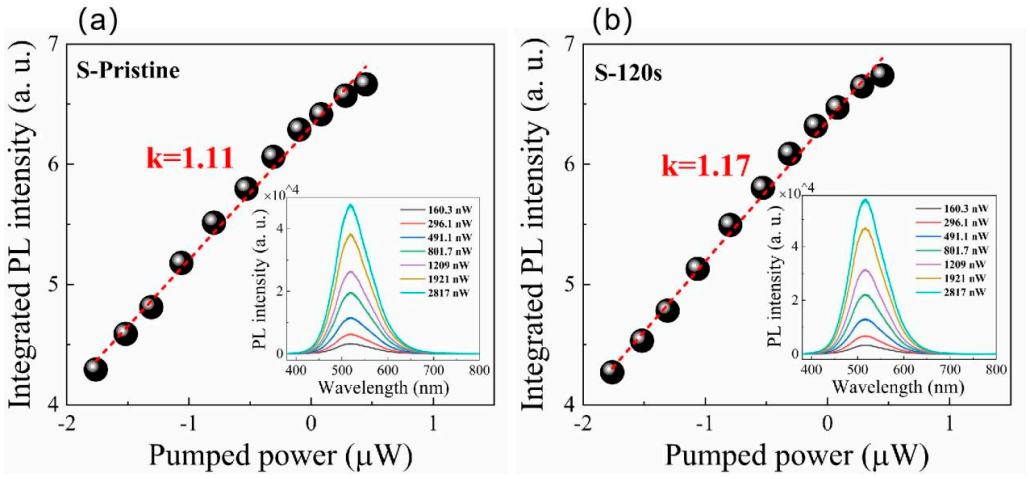

Preprints (www.preprints.org) | NOT PEER-REVIEWED | Posted: 4 July 2023 doi:10.20944/preprints202307.0071.v1

Figure 2. The integrated PL intensity under different excitation powers: (a) pristine sample, (b) sample-120s. The red solid lines are theoretical fitting curves. Insets in Figure 2a and 2b show the PL spectra from pristine sample and sample-120s under different excitation powers, respectively.

To understand the enhanced PL, the structure and compositions of Cs_4SnBr_6 samples were evaluated via SEM and EDS, respectively. Figure 3(a) showcases the SEM image obtained from the pristine Cs_4SnBr_6 sample. The EDS spectrum reveals the presence of Cs, Sn, Br, and F elements in Cs_4SnBr_6, which are uniformly distributed, as demonstrated in the EDS mapping of Figure 3(c)-3(f). The Cs, Sn, Br, and F elements maintain this uniform distribution even after Cs_4SnBr_6 was annealed at an RTT temperature of 200°C for a duration of 120 s, as shown in Figure 4(c)-4(f). This result indicates that the elemental distribution of Cs_4SnBr_6 remained unaltered when subjected to RTT at 200°C for a duration of 120 s.

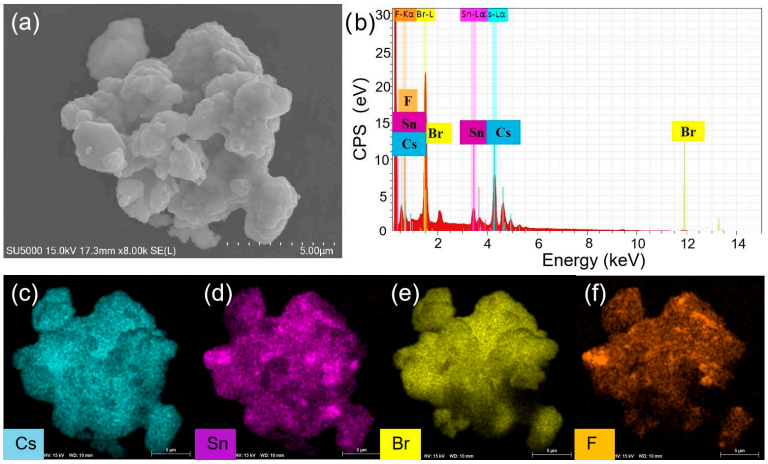

Figure 3. (a) SEM image, (b) EDS spectrum, and (c)-(f) EDS elemental maps of Cs, Sn, Br, and F for a typical pristine Cs_4SnBr_6 sample, respectively.

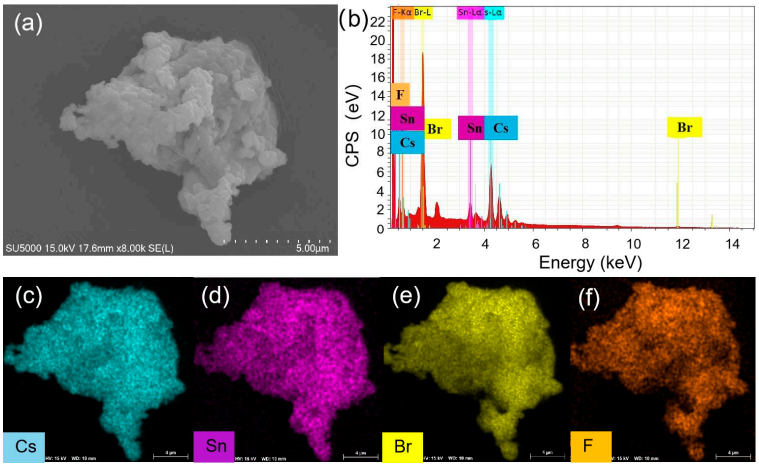

Figure 4. (a) SEM image, (b) EDS spectrum, and (c)-(f) EDS elemental maps of Cs, Sn, Br, and F for Cs_4SnBr_6 sample S-120s annealed at a RTT temperature of 200°C for 120 s, respectively.

In Figure 5, we present the XRD patterns obtained for different samples. The XRD pattern of pristine Cs_4SnBr_6 sample (S-0s) reveals the coexistence phase of Cs_4SnBr_6 and CsBr due to incomplete consumption of CsBr powder precursors in the solid-state reaction. Apart from the prominent diffraction peak at 29.7°, attributed to the CsBr phase, we observe that the diffraction peaks of S-0s from the Cs_4SnBr_6 phase are consistent with those reported for Cs_4SnBr_6-SnF_2[19,34]. This consistency suggests that the substitution of Br^- with smaller F^- effectively suppresses the oxidation of Sn^{2+} in Cs_4SnBr_6. Notably, the diffraction peaks corresponding to crystal planes (110), (300), (131), (223), and (330) of the Cs_4SnBr_6 phase become more pronounced and well-defined as the RTT time increases

Preprints (www.preprints.org) | NOT PEER-REVIEWED | Posted: 4 July 2023 doi:10.20944/preprints202307.0071.v1

from 0 s to 120 s [34]. This strongly indicates an enhanced crystallinity of the Cs_4SnBr_6 powders after the RTT process.

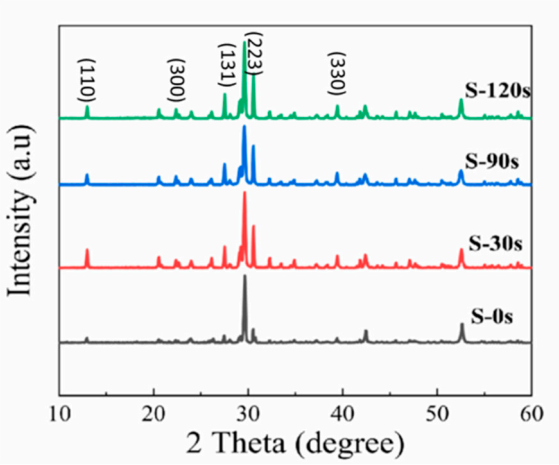

Figure 5. XRD patterns of the pristine Cs_4SnBr_6 sample and the samples annealed at a RTT temperature of 200°C for 30s, 90s, and 120s, respectively.

To better comprehend the PL characteristics, we employed an excitation wavelength of 375 nm (facilitated by 70 ps excitation pulses from a laser) to measure the PL decay curves, as illustrated in Figure 6. The PL decay curve associated with the green emission yielded a sound fit when we employed a biexponential decay function [35]:

$$I(t) = I_0 + A_1 exp\left(\frac{-t}{\tau_1}\right) + A_2 exp\left(\frac{-t}{\tau_2}\right) \quad (1)$$

where I_0 represents the background level, τ_1 and τ_2 represent the lifetimes of each exponential decay component, and A_1 and A_2 denote the corresponding amplitudes. The intensity-weighted averaged PL lifetimes are then determined by $(A_1 * \tau_1^2 + A_2 * \tau_2^2)/(A_1 * \tau_1 + A_2 * \tau_2)$ [35]. As depicted in Figure 6, the green emission in all samples exhibits a slow decay with a long radiative lifetime of approximately 1 μs. Notably, the lifetime remains nearly unchanged despite variations in the RTT conditions, even though the crystallinity of the Cs_4SnBr_6 samples improves after the RTT process. These findings suggest that the PL enhancement does not exclusively arise from a reduction in nonradiative recombination centers.

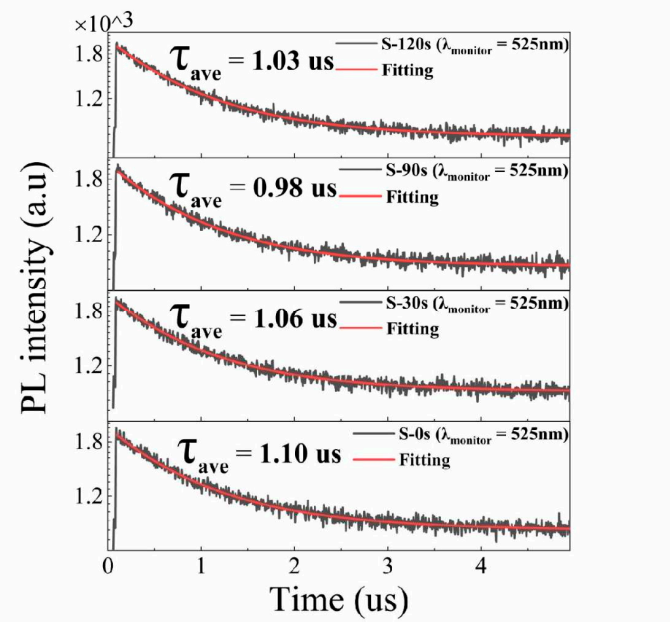

Preprints (www.preprints.org) | NOT PEER-REVIEWED | Posted: 4 July 2023 doi:10.20944/preprints202307.0071.v1

Figure 6. Time-resolved PL decay traces, captured at 525 nm, in both the pristine Cs_4SnBr_6 sample and the samples subjected to annealing at a RTT temperature of 200°C for varying durations. Each measurement was conducted under an excitation wavelength of 375 nm, employing 70 ps excitation pulses from a laser.

In order to gain insights into the influence of electron-phonon coupling, the temperature-dependent PL spectra of the samples were measured in the range of 100 to 300 K. As shown in Figure 7(a) and (b), a decrease in temperature led to an increase in PL intensity and a reduction in the FWHM for both the pristine sample and sample-120s. According to the theory proposed by Stadler [36], the FWHM of the PL peak is closely related to the electron-phonon coupling and can be described by the following equation:

$$FWHM(T) = 2.36\sqrt{S}\hbar\omega\sqrt{\coth\frac{\hbar\omega}{2k_BT}} \quad (2)$$

where S is the Huang-Rhys factor, $\hbar\omega$ is the energy of the phonon mode, T is the temperature, and k_B is Boltzmann's constant. By fitting the temperature-dependent FWHM of the PL peaks using the equation 2, we can calculate the value of the Huang-Rhys factor S, which is commonly used to describe the exciton-phonon coupling. For the pristine sample, it was found that the value of S is as large as 63.7 (see Figure 7(c)), which is significantly higher than that reported in Cs_4SnBr_6. Generally, a larger S value indicates a stronger electron-phonon coupling, which is more favorable for the formation of STEs. However, a high S value also increases the probability of non-radiative recombination [24]. The Raman spectrum shown in the inset of Figure 7(c) reveals two dominant phonon modes, corresponding to the Sn-Br stretching vibrational modes at approximately 130 cm^{-1} and 220 cm^{-1} [37,38], respectively, which may be involved in the electron-phonon coupling and thus result in the S value as large as 63.7. After annealing the sample at a RTT temperature of 200°C for 120 s, the value of S is significantly reduced to 46.1, which closely resembles that observed in Cs_4SnBr_6 [28]. This reduction can be attributed to the disappearance of the Sn-Br stretching vibrational mode near 240 cm^{-1} (see the inset of Figure 7(d)) resulting from the enhanced crystallinity of the Cs_4SnBr_6 powders after the RTT process, as evidenced by the X-ray diffraction (XRD) patterns (refer to Figure 5). The fitted data in Figure 7(d) provide an optical phonon energy (E_{LO}) of 16.7 meV (134 cm^{-1}), which corresponds well with the Sn-Br stretching vibrational mode near 130 cm^{-1} in Cs_4SnBr_6 (see the inset of Figure 7(d)) [37,38]. This suggests that the electron-phonon coupling only involves the dominant phonon mode near 130 cm^{-1}, which corresponds to the Sn-Br stretching vibrational mode near 130 cm^{-1}. On another note, the PL QY of STEs highly depends on the exciton binding energy. The detrapping of STEs due to thermal activation results in a decreased radiative recombination rate. The exciton binding energy of STEs can be determined by analyzing the temperature-dependent integrated PL intensity (I_{PL}) using the Arrhenius equation [33]:

$$I_{PL}(T) = \frac{I_{PL}(T_0)}{1 + \beta exp(-E_b/k_B T)} \quad (3)$$

where $I_{PL}(T_0)$ is the integrated PL intensity at 80 K, β is a constant related to the density of radiative recombination centers, k_B is Boltzmann's constant, and E_b is the exciton binding energy. Through fitting the experimental data with the Arrhenius equation, we can obtain the exciton binding energy E_b of 227 meV and 409 meV for the pristine sample and sample S-120, respectively (see Figure 7(e) and Figure 5(f)). It is noteworthy that the E_b value in sample S-120 substantially exceeds the 227 meV found in the pristine sample. This infers that the detrapping of STEs via thermal activation has been effectively suppressed in sample S-120, resulting in an augmented emission from the STEs. Therefore, based on the above analyses, we deduce that optimal electron-phonon coupling, compounded by the enhanced exciton binding energy elicited by the RTT, is responsible for the enhanced STE emission discerned in sample S-120.

Preprints (www.preprints.org) | NOT PEER-REVIEWED | Posted: 4 July 2023 doi:10.20944/preprints202307.0071.v1

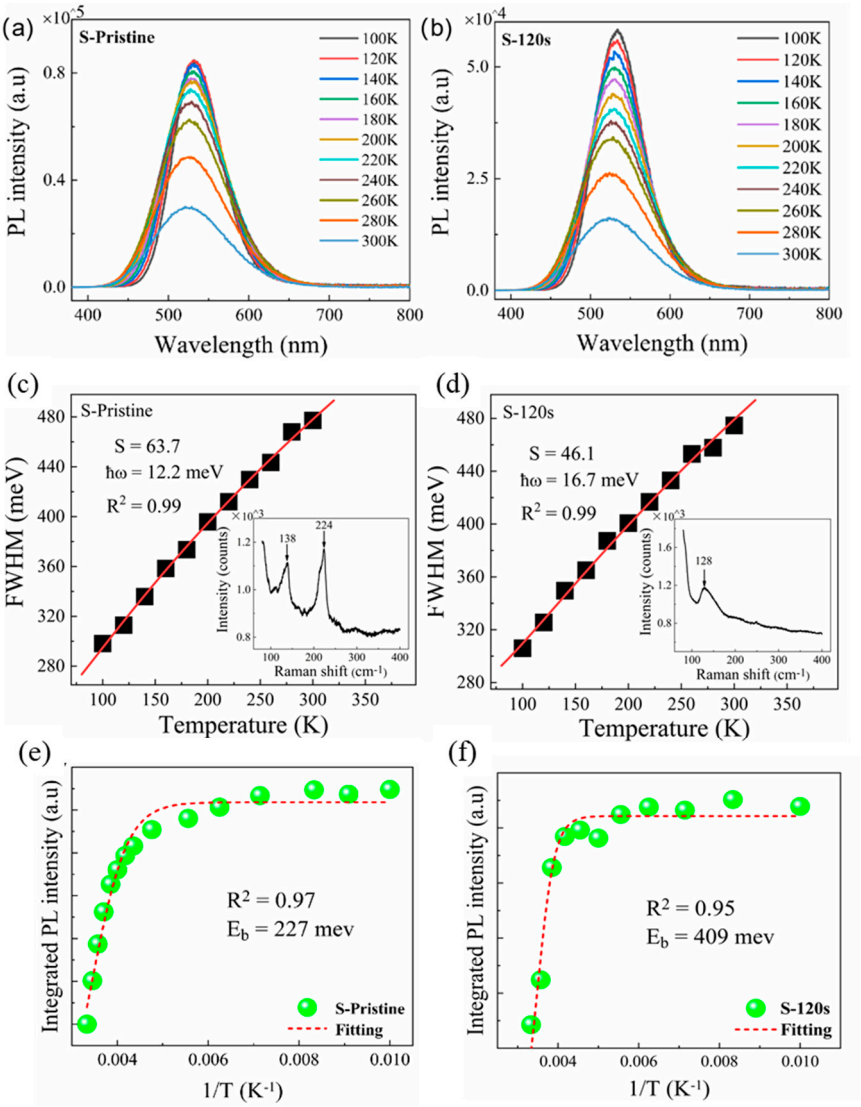

Figure 7. Temperature-dependent PL spectra measured in the range of 100 to 300 K for (a) pristine sample, (b) sample S-120s annealed at a RTT temperature of 200°C for 120 s. Temperature-dependent PL linewidth observed for (c) pristine sample and (d) sample S-120s (solid symbols), and the fitting of the experimental data (red line) by using Eq. (1). The insets in Figure (c) and (d) show the Raman spectrum of pristine sample and sample S-120s, respectively. Integrated PL intensities measured for (e) pristine sample and (f) sample S-120s at different temperatures (green solid symbols). Also shown is the fitting of the corresponding experimental data (red dashed curve) of the pristine sample and sample S-120s.

4. Conclusions

In conclusion, our study systematically investigated the impact of RTT on the PL properties of lead-free Cs_4SnBr_6. The results showed that RTT at 200°C for 120 seconds significantly enhanced the emission from STEs, with the photoluminescence quantum yield increasing up to 64.7%. Through analysis of temperature-dependent PL spectra, Raman spectra, and PL decay traces, we propose that the improvement in photoluminescence is due to appropriate electron-phonon coupling and increased binding energies of STEs induced by the RTT. Our study offers a new approach for the development of efficient luminescent 0D tin-halide perovskites, which holds significant implications for the future advance.

Author Contributions: H.W. (Haixia Wu): investigation, formal analysis, writing - original draft. Z.L.: investigation, formal analysis. J.Song.: investigation. Y.Z.: investigation, Y.G.: investigation, W.Z.: investigation,

R.H.: writing—review and editing, formal analysis, funding acquisition. All authors have read and agreed to the published version of the manuscript.

Funding: This research was funded by the Guangdong Basic and Applied Basic Research Foundation (2020A1515010432), Project of Guangdong Province Key Discipline Scientific Research Level Improvement (2021ZDJS039, 2022ZDJS067), Special Innovation Projects of Guangdong Provincial Department of Education (2019KTSCX096, 2020KTSCX076), Advanced Materials and Devices Laboratory(623012).

Data Availability Statement: Data underlying the results presented in this paper are not publicly available at this time but may be obtained from the authors upon reasonable request.

Conflicts of Interest: The authors declare no conflict of interest.

References

1. Li, M.; Xia, Z. Recent progress of zero-dimensional luminescent metal halides. *Chem. Soc. Rev.* **2021**, *50*, 2626-2662.
2. Akkerman, Q.A.; Abdelhady, A. L.; Manna, L. Zero-dimensional cesium lead halides: history, properties, and challenges. *J. Phys. Chem. Lett.* **2018**, *9*, 2326–2337.
3. Zhou, C.; Xu, L.J.; Lee, S.; Lin, H.; Ma, B. Recent Advances in Luminescent Zero-Dimensional Organic Metal Halide Hybrids. *Adv. Opt. Mater.* **2021**, *9*, 2001766.
4. Sun, S.; Lu, M.; Gao, X.; Shi, Z.; Bai, X.; Yu, W.W.; Zhang, Y. 0D perovskites: Unique properties, synthesis, and their applications. *Adv. Sci.* **2021**, *8*, 2102689.
5. Yakunin, S.; Benin, B.M.; Shynkarenko, Y.; Nazarenko, O.; Bodnarchuk, M.I.; Dirin, D.N.; Hofer, C.; Cattaneo, S.; Kovalenko, M.V. High-resolution remote thermometry and thermography using luminescent low-dimensional tin-halide perovskites. *Nat. Mater.* **2019**, *18*, 846-852.
6. Tan, Z.; Chu, Y.; Chen, J.; Li, J.; Ji, G.; Niu, G.; Gao, L.; Xiao, Z.; Tang, J. Lead-free perovskite variant solid solutions $Cs_2Sn_{1-x}Te_xCl_6$: bright luminescence and high anti-water stability. *Adv. Mater.* **2020**, *32*, 2002443.
7. Chang, T.; Wei, Q.; Zeng, R.; Cao, S.; Zhao, J.; Zou, B. Efficient energy transfer in Te^{4+}-doped Cs_2ZrCl_6 vacancy-ordered perovskites and ultrahigh moisture stability via A-site Rb-alloying strategy. *J. Phys. Chem. Lett.* **2021**, *12*, 1829–1837.
8. Chen, D.; Wan, Z.; Chen, X.; Yuan, Y.; Zhong, J. Large-scale room-temperature synthesis and optical properties of perovskite-related Cs_4PbBr_6 fluorophores. *J. Mater. Chem. C* **2016**, *4*, 10646-10653.
9. Fan, Q.; Biesold-McGee, G.V.; Ma, J.; Xu, Q.; Pan, S.; Peng, J.; Lin, Z. Lead-free halide perovskite nanocrystals: crystal structures, synthesis, stabilities, and optical properties. *Angew. Chem. Int. Ed.* **2020**, *59*, 1030-1046.
10. Li, X.; Gao, X.; Zhang, X.; Shen, X.; Lu, M.; Wu, J.; Shi, Z.; Colvin, V.L.; Hu, J.; Bai, X.; Yu, W.W.; Zhang, Y. Lead-Free Halide Perovskites for Light Emission: Recent Advances and Perspectives. *Adv. Sci.* **2021**, *8*, 2003334.
11. Wang, A.; Guo, Y.; Zhou, Z.; Niu, X.; Wang, Y.; Muhammad, F.; Li, H.; Zhang, T.; Wang, J.; Nie, S.; Deng, Z. Aqueous acid-based synthesis of lead-free tin halide perovskites with near-unity photoluminescence quantum efficiency. *Chem. Sci.* **2019**, *10*, 4573-4579.
12. Wang, X.; Zhang, T.; Lou, Y.; Zhao, Y. All-inorganic lead-free perovskites for optoelectronic applications. *Mater. Chem. Front.* **2019**, *3*, 365-375.
13. Liu, Q.; Yin, J.; Zhang, B.B.; Chen, J.K.; Zhou, Y.; Zhang, L.M.; Wang, L.M.; Zhao Q.; Hou, J.; Shu, J.; Song, B.; Shirahata, N.; Bakr, O.M.; Mohammed, O.F.; Sun, H.T. Theory-guided synthesis of highly luminescent colloidal cesium tin halide perovskite nanocrystals. *J. Am. Chem. Soc.* **2021**, *143*, 5470-5480.
14. Benin, B.M.; Dirin, D.N.; Morad, V.; Wörle, M.; Yakunin, S.; Rainò, G.; Nazarenko, O.; Fischer, M.; Infante, I.; Kovalenko, M. V. Highly emissive self-trapped excitons in fully inorganic zero-dimensional tin halides. *Angew. Chem. Int. Ed.* **2018**, *57*, 11329-11333.
15. Zhang, X.; Wang, H.; Wang, S.; Hu, Y.; Liu, X.; Shi, Z.; Colvin, V.L.; Wang, S.; Yu, W.W.; Zhang, Y. Room temperature synthesis of all inorganic lead-free zero-dimensional Cs_4SnBr_6 and Cs_3KSnBr_6 perovskites. *Inorg. Chem.* **2019**, *59*, 533-538.
16. Tan, L.; Wang, W.; Li, Q.; Luo, Z.; Zou, C.; Tang, M.; Zhang, L.; He, J.; Quan, Z. Colloidal syntheses of zero-dimensional Cs_4SnX_6 (X= Br, I) nanocrystals with high emission efficiencies. *Chem. Commun.* **2020**, *56*, 387-390.

17. Jellicoe, T.C.; Richter, J.M.; Glass, H.F.; Tabachnyk, M.; Brady, R.; Dutton, S.E.; Rao, A.; Friend, R.H.; Credgington, D.; Greenham, N.C.; Bo¨hm, M.L. Synthesis and optical properties of lead-free cesium tin halide perovskite nanocrystals. *J. Am. Chem. Soc.* **2016**, *138*, 2941–2944.
18. Kang, C.; Rao, H.; Fang, Y.; Zeng, J.; Pan, Z.; Zhong, X. Antioxidative stannous oxalate derived lead-free stable $CsSnX_3$ (X= Cl, Br, and I) perovskite nanocrystals. *Angew. Chem. Int. Ed.* **2021**, *60*, 660-665.
19. Zhang, Q.; Liu, S.; He, M.; Zheng, W.; Wan, Q.; Liu, M.; Liao, X.; Zhan, W.; Yuan, C.; Liu, J.; Xie, H.; Guo, X.; Kong, L.; Li, L. Stable Lead-Free Tin Halide Perovskite with Operational Stability > 1200 h by Suppressing Tin (II) Oxidation. *Angew. Chem. Int. Ed.* **2022**, *61*, e202205463.
20. Zhou, C.; Lin, H.; He, Q.; Xu, L.; Worku, M.; Chaaban, M.; Lee, S.; Shi, X.; Du, M.H.; Ma, B. Low dimensional metal halide perovskites and hybrids. *Mater. Sci. Eng. R Rep.* **2019**, *137*, 38-65.
21. Smith, M.D.; Connor, B.A.; Karunadasa, H.I. Tuning the luminescence of layered halide perovskites. *Chem. Rev.* **2019**, *119*, 3104–3139.
22. Lin, H.; Zhou, C.; Tian, Y.; Siegrist, T.; Ma, B. Low-dimensional organometal halide perovskites. *ACS Energy Lett.* **2017**, *3*, 54–62.
23. Hu, T.; Smith, M.D.; Dohner, E.R.; Sher, M.J.; Wu, X.; Trinh, M.T.; Fisher, A.; Corbett, J.; Zhu, X.Y.; Karunadasa, H.I.; Lindenberg, A.M. Mechanism for broadband white-light emission from two-dimensional (110) hybrid perovskites. *J. Phys. Chem. Lett.* **2016**, *7*, 2258–2263.
24. Li, S.; Luo, J.; Liu, J.; Tang, J. Self-trapped excitons in all-inorganic halide perovskites: fundamentals, status, and potential applications. *J. Phys. Chem. Lett.* **2019**, *10*, 1999–2007.
25. Dohner, E.R.; Jaffe, A.; Bradshaw, L.R.; Karunadasa, H.I. Intrinsic white-light emission from layered hybrid perovskites. *J. Am. Chem. Soc.* **2014**, *136*, 13154–13157.
26. Han, P.; Luo, C.; Yang, S.; Yang, Y.; Deng, W.; Han, K. All-inorganic lead-free 0D perovskites by a doping strategy to achieve a PLQY boost from< 2% to 90%. *Angew. Chem.* **2020**, *132*, 12809-12813.
27. Ma, Z.; Liu, Z.; Lu, S.; Wang, L.; Feng, X.; Yang, D.; Wang, K.; Xiao, G.; Zhang, L.; Redfern, S.A.; Zou, B. Pressure-induced emission of cesium lead halide perovskite nanocrystals. *Nat. Commun.* **2018**, *9*, 4506.
28. Ulloa, J.M.; Llorens, J.M.; Alén, B.; Reyes, D.F.; Sales, D.L.; González, D.; Hierro, A. High efficient luminescence in type-II GaAsSb-capped InAs quantum dots upon annealing. *Appl. Phys. Lett.* **2012**, *101*, 253112.
29. Lin, Z.; Wang, A.; Huang, R.; Wu, H.; Song, J.; Lin, Z.; Hou, D.; Zhang, Z.; Guo, Y.; Lan, S. Manipulating the sublattice distortion induced by Mn^{2+} doping for boosting the emission characteristics of self-trapped excitons in Cs_4SnBr_6. *J. Mater. Chem. C* **2023**, *11*, 5680-5687.
30. Bergman, L.; Chen, X.B.; Morrison, J.L.; Huso, J.; Purdy, A.P. Photoluminescence dynamics in ensembles of wide-band-gap nanocrystallites and powders. *J. Appl. Phys.* **2004**, *96*, 675-682.
31. Guo, Q.; Zhao, X.; Song, B.; Luo, J.; Tang, J. Light Emission of Self-Trapped Excitons in Inorganic Metal Halides for Optoelectronic Applications. *Adv. Mater.* **2022**, *34*, 2201008.
32. Sun, C.; Jiang, K.; Han, M.F.; Liu, M.J.; Lian, X.K.; Jiang, Y.X.; Shi, H.S.; Yue, C.Y.; Lei, X.W. A zero-dimensional hybrid lead perovskite with highly efficient blue-violet light emission. *J. Mater. Chem. C* **2020**, *8*, 11890-11895.
33. Wang, X.; Zhang, X.; Yan, S.; Liu, H.; Zhang, Y. Nearly-Unity Quantum Yield and 12-Hour Afterglow from a Transparent Perovskite of $Cs_2NaScCl_6$: Tb. *Angew. Chem. Int. Ed.* **2022**, *61*, e202210853.
34. Chiara, R.; Ciftci, Y.O.; Queloz, V.I.; Nazeeruddin, M.K.; Grancini, G.; Malavasi, L. Green-emitting lead-free Cs_4SnBr_6 zero-dimensional perovskite nanocrystals with improved air stability. *J. Phys. Chem. Lett.* **2020**, *11*, 618-623.
35. Lin, K.H.; Liou, S.C.; Chen, W.L.; Wu, C.L.; Lin, G.R.; Chang, Y.M. Tunable and stable UV-NIR photoluminescence from annealed SiO_x with Si nanoparticles. *Opt. Express* **2013**, *21*, 23416-23424.
36. Stadler, W.; Hofmann, D.M.; Alt, H.C.; Muschik, T.; Meyer, B.K.; Weigel, E.; Müller-Vogt, G.; Salk, M.; Rupp, E.; Benz, K.W. Optical investigations of defects in $Cd_{1-x}Zn_xTe$. *Phys. Rev. B* **1995**, *51*, 10619.

37. Kuok, M.H.; Tan, L.S.; Shen, Z.X.; Huan, C.H.; Mok, K.F. A Raman study of $RbSnBr_3$. *Solid State Commun.* **1996**, *97*, 497-501.
38. Qin, Z.; Dai, S.; Hadjiev, V.G.; Wang, C.; Xie, L.; Ni, Y.; Wu, C.; Yang, G.; Chen, S.; Deng, L.; Yu, Q.; Feng, G.; Wang, Z.M.; Bao, J. Revealing the origin of luminescence center in 0D Cs_4PbBr_6 perovskite. *Chem. Mater.* **2019**, *31*, 9098–9104.